The Influence of Alloy Disorder Effects on the Anisotropy of Emission Diagrams in (Al,Ga)N Quantum Wells Embedded into AlN Barriers

Alexandra Ibanez, Mathieu Leroux, Nikita Nikitskiy, Wilfried Desrat, Matthieu Moret, Pierre Valvin, Guillaume Cassabois, Julien Brault, Bernard Gil, Fumiya Chugenji, et al.

The influence of alloy disorder effects on the anisotropy of emission diagrams in (Al,Ga)N Quantum Wells embedded into AlN barriers

*Alexandra Ibanez[1], Mathieu Leroux[2], Nikita Nikitskiy[2], Wilfried Desrat[1],Matthieu Moret[1], Pierre Valvin[1], Guillaume Cassabois[1], Julien Brault[2], and Bernard Gil[1]**

1-Laboratoire Charles Coulomb, CNRS, Université de Montpellier, Montpellier F-34095, France

2- Université Côte d'Azur, CNRS, CRHEA, Rue Bernard Gregory, F-06560 Valbonne, France

Fumiya Chugenji, Kirihara Taiga, M. Ajmal Khan, and Hideki Hirayama

RIKEN Cluster for Pioneering Research (CPR), 2-1 Hirosawa, Wako, Saitama 351-0198, Japan

** Corresponding author: Bernard.gil@umontpellier.fr*

Keywords: deep ultraviolet emission, wide bandgap semiconductors, aluminum nitride

ABSTRACT

We measure the shapes of the photoluminescence (PL) emitted on the edge of a series of aluminum-rich (Al,Ga)N-AlN quantum wells (QWs) grown by Molecular Beam Epitaxy on AlN templates deposited by Metal Organic Chemical Vapour Deposition on c-plane sapphire. We study the shape and the spatial orientation of the emission diagrams for 2 nm-thick (Al,Ga)N QWs grown for aluminum compositions ranging between 40 and 90 percent. The light emitted on the edge of the QWs at wavelengths going from 280 nm down to 209 nm is characterized by a switching of the orientation of the long axis of the emission diagram, a change from oblate to prolate in the in-plane orientation for an aluminum composition is found to occur around 72 % i.e. at a wavelength of about 235nm. The orientations and shapes of the edge emission diagrams indicate that the composition-dependent fluctuations of the (Al,Ga)N confining layer are deep enough for producing intra-valence-band mixings. This property, that act in concert with the built-in strain and Quantum Confined Stark Effect contributes to the anisotropy of the light emission when the aluminum composition reaches 60-70 percent (i.e. for an emission wavelength of 260-235 nm).

1. Introduction

There have been a lot of motivations for many years now, in order to realize efficient compact solid state light emission devices emitting radiations in the 400-200 nm range or ultraviolet (UV) part of the electromagnetic spectrum **[1]**. This activity has stimulated applications in the fields of information technologies, high resolution imaging, food industry. They are now extending towards the areas of clinical and fundamental biology**[**2**].** We wish to emphasize that, in contrast with the other UV radiations, ultraviolet of the C type (UVC) radiations with wavelengths near 230 nm, do not penetrate deep into the skin and this prevents them to provoke unwanted (and sometimes deleterious) burnings of the sane tissues of an organ under a photo-medical treatment **[3-6]** , while intercepting efficiently the targeted pathogen agent. The complexity of the biological science requires different wavelengths with different penetration depths of the radiations to eradicate the large variety of pathogen targets of interest. As an example UV light at 220-230 nm (UVC) has a shallow penetration depth, and inactivates viruses (it can destroy DNA and proteins of the viruses' cell membrane which sizes are in general below 0.1 μm in diameter). It cannot penetrate deep and provoke damage to human skin cells that are much bigger, of the order of 10-30 μm in diameter. Wavelengths shorter than 222 nm have a very shallow penetration depth that prevents them from penetrating into corneas, the outermost layer of human eyes and this is useful for surface treatments of the stratum corneum. Besides, and still considering ophthalmology, wavelengths above 230 nm penetrate deeper in the eyes. Therefore, UVC lights of 254-270 nm wavelengths have to be used very carefully as they are able to damage the eyes and for instance can enforce incurable diseases like macular degeneration.

The group III element nitrides semiconductors are the basic building blocks of this UVC technology currently under intense consideration. The relevant material for that purpose is an aluminum-rich solid solution of (Al,Ga)N with a controlled metallic composition. Various compositions of such an alloy (and eventually the binary phase AlN) are assembled together to form semiconductor heterostructures that are at the heart of UVC light emitting devices**[**7**]** . However, to realize such devices, it not only required to extend mutatis mutandis the *mature* technology of blue light emitting diodes (LEDs) based on GaN alloyed with indium to the (Al,Ga)N alloys. There are specific issues linked to (Al,Ga)N, like there are also obviously specific ones linked to (In,Ga)N. For the (In,Ga)N route, the main technological solutions have been found. The processes are almost routine and the real issue seems today to sit in the area

of ultimate optimizations. The electrical injection in the active (In,Ga)N layer(s) is currently the subject of sophisticated quantitative numerical modellings beyond the scope of the effective mass approximation**[8-12]**.

Regarding UV and (Al,Ga)N-related devices, the electrical injection requires different technologies for contacting both sides of the active part of the LED**[13]** that are not fully controlled at the time being. Although contacting the n-type is fairly easy, this is absolutely not the case for the p-type layer**[14]** . To make the story short here, due to the increasing localization energy of the p dopant Mg in (Al,Ga)N with increasing the Al composition **[15,16],** a limited amount of the incorporated Mg impurities is electrically active. The Mg-doped layer is modestly p-type, and the ohmic contact with an ad-hoc metal generally exhibits very poor performances. As a result, part of the electric injection energy is transformed into heat with deleterious influences on the lifetime of the contact**[17] .**

Again, to target the range of small wavelengths, aluminum barrier layers and an aluminum substrate (or a pre-prepared pseudo substrate) are required. The growth of such materials has not reached the degree of perfection of the growth of GaN, although considerable progresses have been made**[18, 19].** The materials are much more defective than those for the blue LED technology, and there are much more losses due to the non-radiative recombination of carriers on dense topological defects.

A specific issue that has been identified for (Al,Ga)N is the switch of the symmetry of the topmost valence band that occurs for a 10-percent aluminum composition in the bulk **[20-22]** and for a 60-percent aluminum composition in (Al,Ga)N lattice-matched to AlN **[23]**. There is then a crossover in the 260 nm range for emission of a TE-polarized (significantly strong) light to a (weak as it is forbidden) TM-polarized one **[24-26],** at a critical composition $\geq$ 60 percent in aluminum in these latter strained-layer nitrides. For shorter wavelengths, a continuous and rapid collapse of the emission intensity is measured that has been interpreted in the context of the elementary **k.p** description in terms of the effects of the valence band symmetry**[27-58]** .

In this article we study the shape and the spatial orientation of the emission diagrams for (Al,Ga)N-AlN quantum wells (QWs) grown for aluminum compositions ranging between 40 and 90 percent, for which light is emitted from 280 nm down to 209 nm. We clearly show from careful photoluminescence measurements on the edge of the quantum well, that the orientation of the long axis of the emission diagram switches from oblate to prolate in the in-plane orientation. By contrast, it turns from prolate to oblate along the growth axis orientation

when the aluminum composition reaches and/or exceeds compositions of 70-75% (for emission wavelengths below about 230 nm), reaching a degree of polarization (DOP) of -71% (resp.-68%) at 219 nm (resp. 209 nm). The emission diagrams recorded on the edge of the samples which emit light around 260 nm are almost cylindrical and/or weakly oblate in the growth direction. The emission diagrams recorded in the growth plane are perfectly cylindrical whatever the aluminum composition. Such a behavior is universal for (Al,Ga)N-AlN heterostructures and it was previously reported for quantum dots (QDs) as well, but the Stranski-Krastanow growth modes of QDs prevented us to grow low dimensional systems with aluminum compositions higher than 70-75 percent **[23].**

We demonstrate experimentally that neither the shapes of the emission diagrams recorded **for edge emission** nor the evolution of the Full-Width at Half Maximum (FWHM) of the photoluminescence (PL) lines can be interpreted quantitatively in the framework of the **k.p** description of the band structure of the QWs. This statement also holds concerning the DOP of the light emitted on the side of the heterostructures. To go further than what has been done before, we have here considered the statistical disorder of Al and Ga incorporation in the metallic sub-lattice in order to interpret qualitatively the evolution of the PL FWHM as a function of the aluminum composition in the QW. This permits to quantitatively implement the predictions of the **k.p** calculation: the **intrinsic** statistical disorder introduces local fluctuations of the energy landscape**[10]** that localize the photo-created excitons in specific parts of the energy landscape of active device **[59,60]**. The amplitude of such spatial fluctuations of the energy landscape increases with the Al content of the (Al,Ga)N alloy, passes to a maximum around 60% aluminum [simultaneously with the occurrence the maximum of intra-valence band mixings due to the built-in stress in the (Al,Ga)N alloy], and decreases till vanishing for AlN**.**

The fluctuations of this energy landscape break the translational symmetry of the lattice at short scale. They can be expanded along appropriate and specific irreducible representations of the wurtzite point symmetry-depending if one considers fluctuations along the growth direction or in the growth plane. These fluctuations of Al composition mix more or less strongly the different valence band states of the simple **k.p** description, based on the theory of translational invariants in the wurtzite symmetry **[23,61,62]** and contribute to the distortion of the shape of the emission diagrams. The effect is found to be particularly strong in the conditions of maximum valence band mixings that is to say for a PL emission near 260 nm. The Internal Quantum Efficiency (IQE) is thus underestimated as well as the External Quantum Efficiency at these wavelengths. Beyond the frame of this semiquantitative description, we come to the

conclusion that full numerical revisitation of the physics of UV emitting III-Nitrides LEDs according to what is applied to blue LEDs is mandatory in order to determine precisely the real IQE and the real performances at a given wavelength.

2. The Growth and Structural Characterization of the Samples

A well-known technique of ammonia (NH_3) pulsed-flow multilayer growth was adopted to grow AlN templates on c-sapphire substrate **[63,64] .** The epitaxial quality of the home grown AlN template on c-sapphire was confirmed by X-ray diffraction (XRD), where the FWHM values of the X-ray diffraction rocking curves (XRCs) along (0002) and (10-12) planes respectively, were reduced to 150 arcsec and 388 arcsec. The total dislocation densities (TDDs) is estimated to be TDDs ~ 1×10^{8} cm^{-2} **[63,64].** The root mean square (RMS) values of the surface morphology were observed by high resolution of Atomic Force Microscopy (AFM), which is remarkably decreased to 0.641 nm, as shown in figures 1(a) and (b). The surface steps and terraces at the atomic resolution level were observed, as shown in figure 1-(b) and the insert of figure 1-(c).

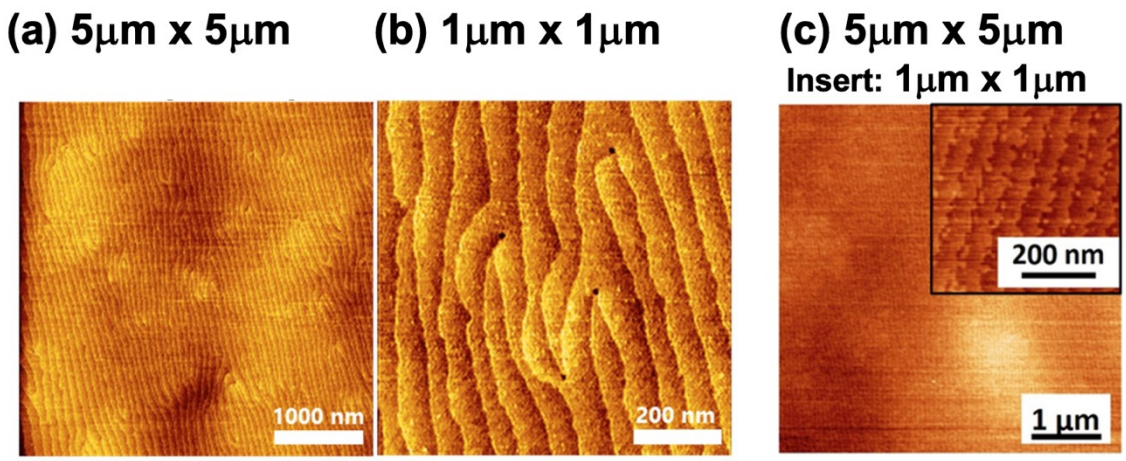

Figure 1: (a) and (b) : AFM images of the surface morphology of AlN template on csapphire substrate with (a) 5 μm×5 μm and (b) 1 μm×1 μm scan areas. (c) AFM image of the surface after the growth of an (Al,Ga)N QW with an aluminum composition of 70%. The scale of the insert of figure 1-(c) is 1 μm×1 μm. The value of the root mean square (RMS) roughness is 0.2 nm with an average terrace width of 70±20 nm.The step height is 1 monolayer.

After the fabrication of the AlN template on sapphire by MOCVD, the sample was introduced into a Molecular Beam Epitaxy (MBE) reactor for the fabrication of $Al_xGa_{1-x}N$ QWs

buried in AlN. At first, a 30-nm thick AlN layer was regrown on the AlN template at a temperature of 870°C in order to prevent from the influence of a possible surface contamination layer. Then, the series of six different QW active regions, with x_{Al} varying from 0.4 to 0.9, was grown as follows: the $Al_xGa_{1-x}N$ layer was deposited at a growth rate of about 0.3 MLs^{-1} and at a temperature ranging between 840°C and 875°C, depending on the x_{Al} value, with the lowest temperature for the $Al_xGa_{1-x}N$ layer with the lowest x_{Al}, and the highest temperature for the $Al_xGa_{1-x}N$ layer with the highest x_{Al}. Finally, a capping layer of 30 nm of AlN was grown and the sample was cooled down before removing it from the MBE reactor. Based on the in-situ RHEED measurement, a diagram made of streaky lines was continuously observed that is characteristic of a 2D growth mode **[23].** The deposited thickness was ranging between 7 to 8 monolayers (MLs), with one ML corresponding to an average thickness of about 0.256 nm. AFM measurements have also been performed to characterize the surface morphology of the structures, showing surfaces made of surface monoatomic steps and smooth terraces, with a typical Root Mean Square (RMS) roughness of 0.2 nm and an average terrace width of 70 ± 20 nm and a step height of 1ML, as indicated in figure 1-(c).

3. The Plate-form of Optical Spectroscopy

The photoluminescence set-up has been described in reference**[23].** The PL signal was excited with the fifth harmonic (corresponding to a wavelength value of 212.8 nm) of a Nd:YAG laser with passive Q-switching, resulting in a pulse width of the order of 1 ns and a repetition rate of 10 kHz. The laser average power on the sample was set to 50 μW. The PL was collected with an achromatic set of off-axis parabolic mirrors. The photoluminescence beam was then collimated and we placed between them a half wave-plate operating between 240 and 300 nm inside a computer-controlled motorized rotation stage. For the excitation of samples with nominal compositions of 78%, 80%, 85% and 90% we used the fourth harmonic of a *cw* mode-locked Ti:Sa oscillator with a repetition rate of 80 MHz tuned at frequency corresponding to a wavelength of 196 nm, and polarization optics that consist in components fabricated by Kogakugiken **[65]** from an MgF_2 single crystal : a Rochon polarizer and a rotating half-wave plate which is achromatic in the spectral range of 160–250 nm, typically.

4. The Quantitative Evidence of the Influence of the Alloy Disorder on the Photoluminescence of Quantum Wells and its Interpretation

In figure 2 are plotted a series of PL spectra recorded at low temperature for Al compositions in the (Al,Ga)N QWs with Al compositions in ranging from 40% up to 90%. The

photo-excitations of the carriers have been realized with two different radiations, namely at 213 nm (corresponding to an excitation energy below the energy of the fundamental gap of the AlN barrier) and at 196 nm for the four highest compositions (corresponding to an excitation energy above the energy of the fundamental bandgap of the AlN barrier). The emission wavelengths of the 78%, 80%, 85% and 90% QWs Al composition are 230 nm, 219 nm, 215 nm and 209 nm respectively on our AlN templates grown on c-sapphire substrate. The PL spectral intensity from an (Al,Ga)N-AlN QWs primarily depends on the crystalline quality of the overall MQWs structure as well as crystal quality of AlN template. The magnification coefficients bridging the two photo-excitation conditions have been obtained using a complementary PL experiment on the 75% Al composition QW. The 230 nm to 200 nm region in figure 2 is very crowded. Please note the PL emission at 205 nm that is identified as the PL related to AlN **[66] .** We remark a rapid collapse of the PL linewidth from 40% until 90%. We also remark the asymmetry of the PL lines towards low energy that is replaced by the clear observation of three (~ 100-110 meV split) phonon replicas for the 78% , 80% and 85% Al composition QW samples (Huang-Rhys factors of 0.60, 0.40 and 0.37 respectively) and only two (Huang-Rhys factor of ~ 0.16) for the 90% Al composition QW sample. Observation in accordance with the decreasing of the signal to noise ratio as visible in figure 2.

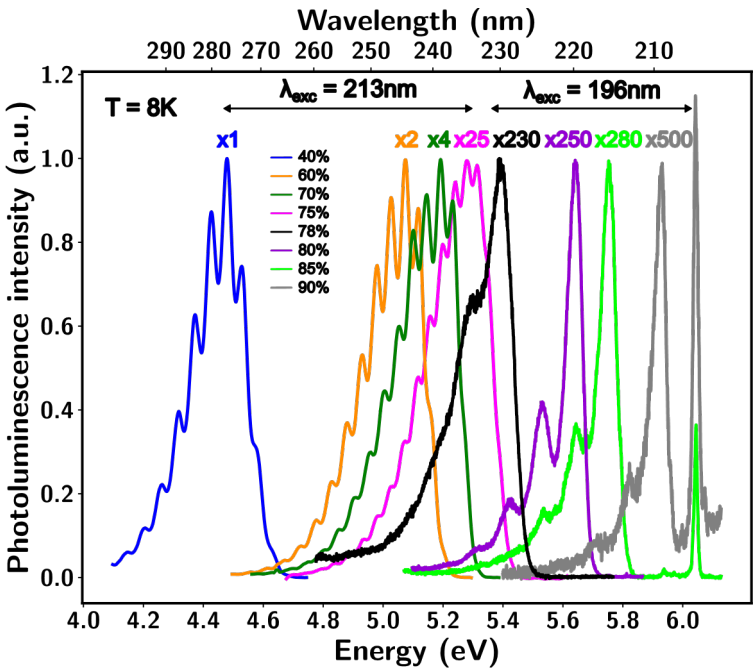

Figure 2: Normalized PL spectra of six QWs for aluminum nominal compositions of the (Al,Ga)N confining alloys of 40% (blue) , 60% (orange), 70% (green) ,75%, (magenta), 78% (dark grey) , 80% (violet), 85%

(green) and 90% (silver). Note the AlN emission at 205 nm. PL spectra were recorded either in conditions of below barrier energy photo-excitation at 213 nm, and above barrier photo-excitation at 196 nm, as indicated in the figure.

The line shape fittings of the PL spectra for samples with 80% and 90 % Al composition QWs are offered in figure 3(a) and 3(b). We interpret the observation of resolved phonon-assisted overtones , not reported so far, on the one hand to the quality of control of the interfaces during the MBE growth protocol on an excellent quality substrate, and on the other hand, in terms of a reduction of alloy broadening effects at high Al composition as will be discussed below. Gaussian fits of the zero PL (ZPL) features are 38 meV, 29 meV, 24 meV and 20 meV for QW samples with Al compositions of 78%, 80% , 85% and 90 % respectively. For the lower Al compositions we have also performed similar Gaussian fits of the zero PL features taking a lot of care for having a close description of the PL shape at the high energy and adding overtones at lower energy for describing the low energy PL wing. From these fits, we can propose the values of the FWHMs of the ZPL for the all compositions that are represented by red spheres in figure 4(a).

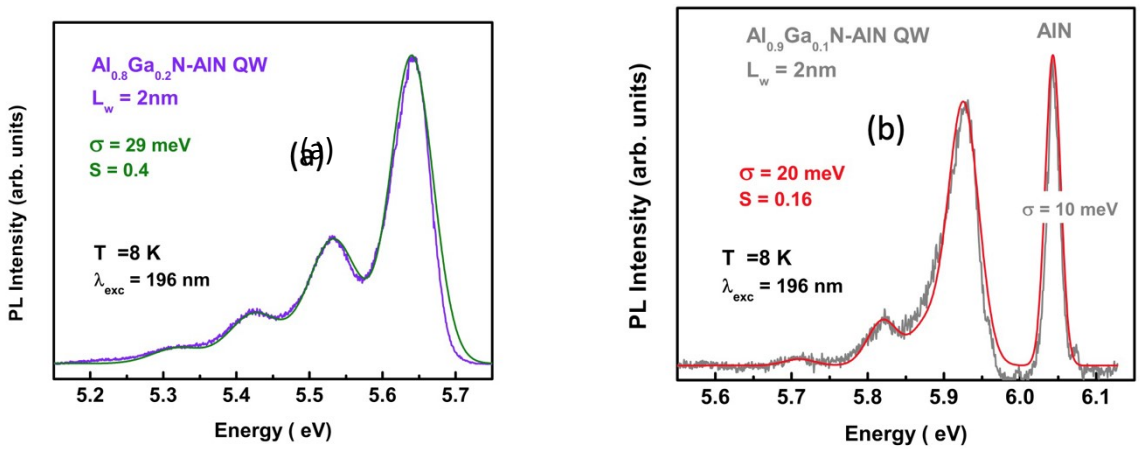

Figure 3: (a) PL spectrum (violet) of the 80% QW and its line-shape fitting (green) using a gaussian function with a value of the σ parameter of 29 meV and Huang-Rhys factor S = 0.4. (b) PL spectrum (silver) of the 90% QW with zero-phonon emission at 209 nm and its line-shape fitting (red) using gaussian function with a value of the σ parameter of 20 meV and Huang-Rhys factor S = 0.16. Please note the narrower AlN emission at 205 nm

In equation (1) is reproduced the theoretical expression of the alloy-induced broadening estimated according to the heuristic method proposed by B.I. Halperin and M. Lax, **[67],** S.D. Baranowski and A.L. Efros **[68]**. This was recently reviewed by S.D.Baranovskii et al. **[69]** for formulating the broadening of the excitonic line probing a disordered material.

$$E_0(x) = \frac{1}{18\pi^2}\frac{\alpha(x)^4 M^3}{\hbar^6 N^2}x^2(1-x^2) \quad (1)$$

In this equation, x and 1-x respectively represent the probability for Al and Ga atoms to randomly occupy one of the site of the metallic sublattice of the $Al_xGa_{1-x}N$ alloy, a(x) represents the derivative of the composition dependence of the bandgap of the $Al_xGa_{1-x}N$ alloy, M is the excitonic mass , and N is the density of atomic sites. There are for instance six III-N formulae in the hexagonal prism of dimensions a and c which leads to the following expression of the density of atomic sites $N = \frac{4}{a^2 c\sqrt{3}}$.

In figure 4 (a) we have plotted the evolution of $E_0(x)$ versus x in blue and magenta for different conditions that will be detailed below and we have plotted using red spheres the evolution of the FWHM the high energy part of the PL features of the (Al,Ga)N QWs. This method permits to get rid of uncontrolled deep defects that are created in the alloy and mask the contributions of the different phonon overtones to the PL in the low energy wing of the PL emission. The numerical calculation in blue was done with the following parameters: $E_g(Al_xGa_{1-x}N) = 6.2x+3.4(1-x) – bx(1-x)$ with b = 0.8±0.2 eV , which gives $\alpha = 2(1+ 0.8x)$; N = 4.38 10^{28} m^{-3} and the value of M was averaged to M = 1.5 in units of the electron mass at rest through the whole composition range. Calculation in magenta corresponds to a bowing parameter b = 0.9 eV. Red spheres represent the evolution of the FWHM of the high energy part of the PL features of the different (Al,Ga)N QWs. To obtain a reasonable picture of what happens in the low aluminum composition range and to get rid of the strong QCSE effect that (Al,Ga)N QWs lattice-matched on AlN experience in such case, making the FWHM to have a dominantly different origin than for the high aluminum composition range **[70-71],** we have also plotted the green spheres that correspond to PL emissions recorded on $2\mu m$-thick non-intentionally doped (Al,Ga)N layers grown by MOVPE on sapphire substrates **[72]**. This data does not depend on the strain at first order, it nicely matches with the calculation, and it substantially enriches the agreement between the experiments and our interpretation below. We remark an astonishing departure of the maximum broadening from the value of 50% obtained by a binomial distribution of atoms. It arises from the nonlinear composition dependence of the bandgap of the GaN and AlN binary compounds and this composition is ruled by the value of the bowing parameter that describes the composition dependence of the band gap of (Al,Ga)N alloy**[73].** Note that in the case of (In,Ga)N, the different values of the bandgaps of the binaries and of the bowing parameter locate this maximum at an indium composition of 20% **[74]**.

In figure 4 (b) we plot the evolution of the valence band energies in (Al,Ga)N alloys lattice-matched to AlN versus the aluminum composition, together with green bars that indicate the theoretical values of the alloy broadening for each of the different nominal compositions of our series of samples. It is worthwhile noticing the large value of the alloy-induced broadening compared to the valence band splitting in the case of lattice-matched (Al,Ga)N QW layers to AlN have dramatic consequences in the 50% to 75% Al composition range, that is to say in the emission wavelength range of 280-230 nm. Indeed, within this range, both alloy broadening effects and built-in strain-induced effects are the most dramatic and act in concert for impacting the whole lightmatter interaction process. Treating such fluctuations of potential as a perturbation of the Bloch states, within the framework of a perturbation for getting meaningful envelope function is not acceptable in the range of compositions when the inter-band splitting is smaller than the disorder-induced perturbation.

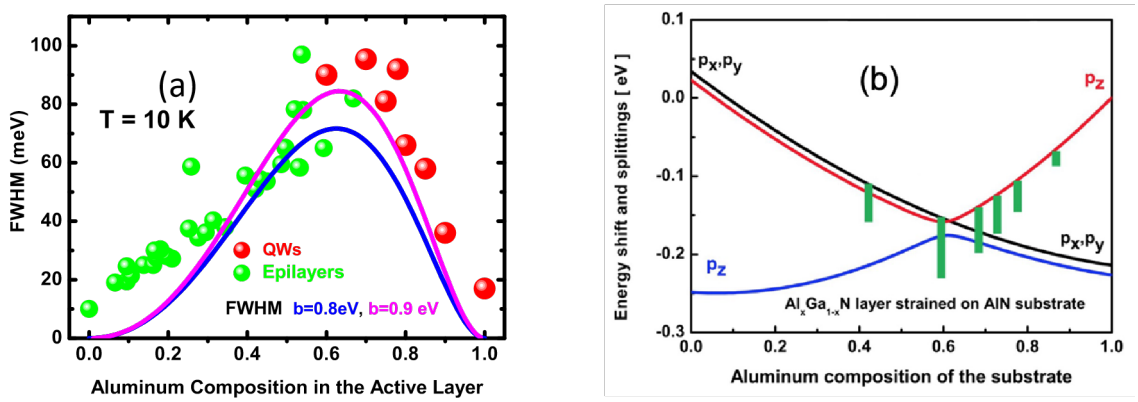

Figure 4: (a) Evolution of the quantity E_0 (x), which characterizes the strength of the alloy-induced broadening obtained using equation 1 (blue). The numerical calculation in blue was done with the following parameters: $E_g(Al_xGa_{1-x}N) = 6.2x+3.4(1-x) – bx(1-x)$ with b = 0.8±0.2 eV , which gives $\alpha = 2(1+ 0.8x)$; N = 4.38 10^{28} m^{-3} and the value of M was averaged to M = 1.5 in units of the electron mass at rest through the whole composition range. Calculation in magenta corresponds to a value of b = 0.9 eV. The red spheres represent the evolution of the FWHM of the high energy part of the PL features of the different (Al,Ga)N QWs. The green spheres correspond to PL emissions recorded on thick non-intentionaly doped AlGaN layers grown by MOVPE on sapphire substrates **[72]**. **(b)** Evolution of the valence band energies versus the aluminum composition in case of (Al,Ga)N lattice-matched to AlN (black, red and blue) together with a representation of the alloy broadening effect (values of E_0) in dark green.

For lower aluminum compositions, the lattice mismatch and the chemical contrasts between (Al,Ga)N and AlN are strong and the huge QCSE combined with unavoidable fluctuations of the thicknesses of the QWs dominate the physics of the FWHM**[70,71].** Potential

screening effects **may** blur the contribution of the alloy disorder. For such compositions time-resolved spectroscopy is much more adapted than *cw* PL for measuring the actual value of the FWHM. For that reason we used when it was possible below barrier energy photo-excitation (213 nm) to limit the absorption of light and the density of photo-created carriers susceptible to diffuse from the barrier layers to the QWs. Quantum wells with lower Al contents, i.e. below 40%, that emit at longer emission wavelengths were thus not studied here.

5. Edge Anisotropy of the Emission Diagrams of these Quantum Wells

A series of emission diagrams recorded the eight (Al,Ga)N QWs samples is offered in figure 5(a), which shows the evolution of the distortion from an Al composition of 40% to an Al composition of90%. The degree of polarization is defined as the fraction:

$$DOP = \frac{I_y - I_z}{I_y + I_z} \quad (2)$$

where I_y and I_z are the PL intensities measured under on-side collection, in the in-plane (y) and on-axis (z) conditions of polarization of the incident photon. It is worthwhile noticing that introducing the half-wave plate and polarizers in MgF_2 (for 78%, 80%, 85% and 90% Al composition QW samples) reduces the PL intensity for intrinsic geometrical reasons and we only obtained the DOP with a large signal to noise ratio that prevents us to accurately measure I_y. Thus, as the -71% value of the DOP measured for the 80% sample is robust [see the spectra in figure 5(b)], the DOP value we propose for the 90% is -68%, but it is probably not consolidated due to the low signal to noise ratio [see figure 5(c)] specifically for the measurement of y-polarized PL. This statement also holds for the DOP of the sample emitting at 215 nm (-56%). Noteworthy, the anisotropy of the PL emission of AlN follows the predictions of the selection rules with a PL intensity that cannot be extracted from the experimental noise in the case of forbidden polarization emission.

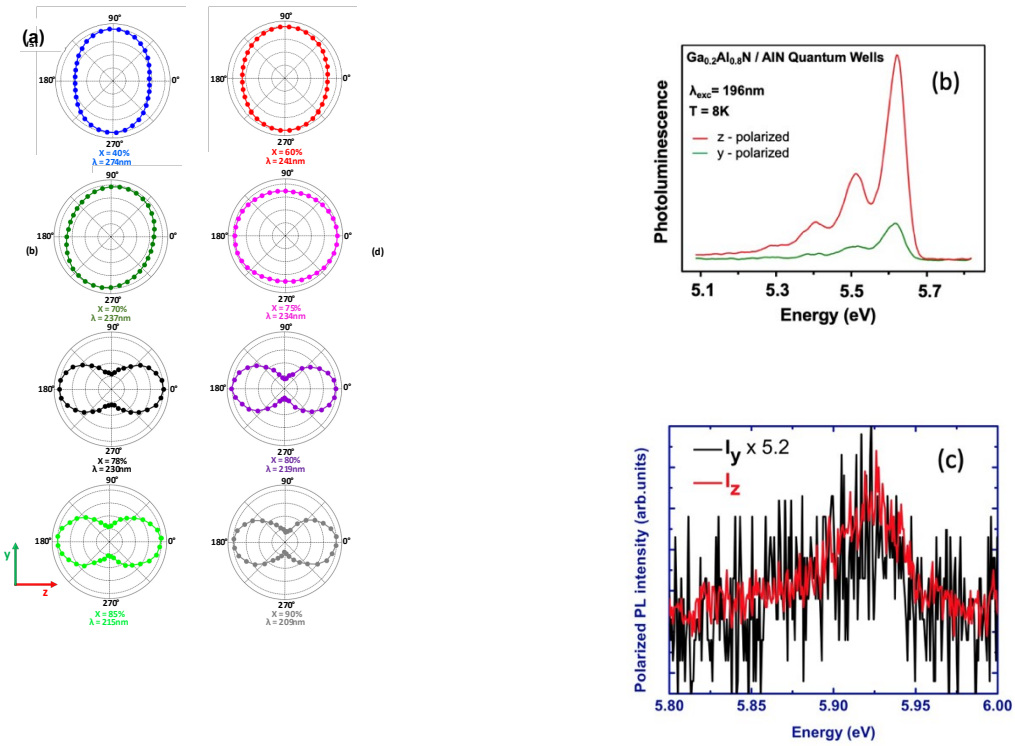

FIGURE 5: (a) Emission diagrams of the QWs with different Al compositions. A similar color code is associated to the different samples in figure 2 and figure 5(a).The directions of the y and z axis are indicated in the left-hand bottom corner. **(b)** Plot of the PL spectra recorded for the 80% Al composition (Al,Ga)N QW sample for the y (green plot) and z (red plot) polarizations of the on-side emission. **(c)** PL emitted under z (red plot) polarization and under y (black plot) polarization conditions. The black feature is magnified by a factor 5.2 which corresponds to a DOP of -68 percent.

In figure 6 is reported the experimental evolution of the DOP reported for our series of (Al,Ga)N QW samples, which are compared to samples grown by MOCVD **[29]**, and by MBE, and MBE-grown QDs **[26]**. The consolidated measurement of the DOP at 219 nm indicates a value of -71%. It means that a substantial amount of the total light emitted on-side with an in-plane polarization of the photon is not emitted as a TE-polarized one in the growth plane **[75]**. The crossover from positive to negative values of the DOP obtained for a well width of 2 nm occurs for a nominal aluminum composition of (Al,Ga)N of about 72% and at a wavelength of 234 nm. This value of the nominal Al composition is the well compatible with what was reported in the pioneering work of Banal et al. **[50]**. They proposed its occurrence for an (Al,Ga)N aluminum composition of 77-78 % in case of a well width of 2 nm (see figure 5 of ref. **[50]**). The dependence they predict for this composition cross-over with well width is evidence of QCSE and is also compatible with the theoretical calculation of Yamaguchi **[24]**. We note an intriguing discrepancy between the degree of polarization reported reference 50 (and represented by purple pentagons in figure 6), and both the works of reference 29 and the present one. In reference 50, two different series of samples are

used. In a first case, the aluminum composition of (Al,Ga)N QWs is fixed at 0.82 and three samples are grown with well widths of thicknesses of 1.3 nm, 8 nm and 13 nm, giving DOPs of 3%, -12% and -17 % respectively (these pentagons are connected by a grey dotted line in Figure 6). It is reasonable to argue that the decrease in the algebraic value of the DOP as the QW thickness increases is related to the Quantum Confined Stark Effect. In the second set of samples, QWs with a similar thickness (about 1.5 nm) and (Al,Ga)N confining layers with aluminum compositions of 0.69, 0.82 and 0.91 are grown, giving DOPs of 7%, 3% and -4 % respectively (these pentagons are connected by a purple dotted line in Figure 6). We note that a reasonable fluctuation of the well width of about 0.2 nm is allowed by the authors, and that the algebraic value of DOP decreases when increasing the aluminum composition in the series of (Al,Ga)N QWs , which corresponds to a decrease of the value of the internal electric field in the active layer.

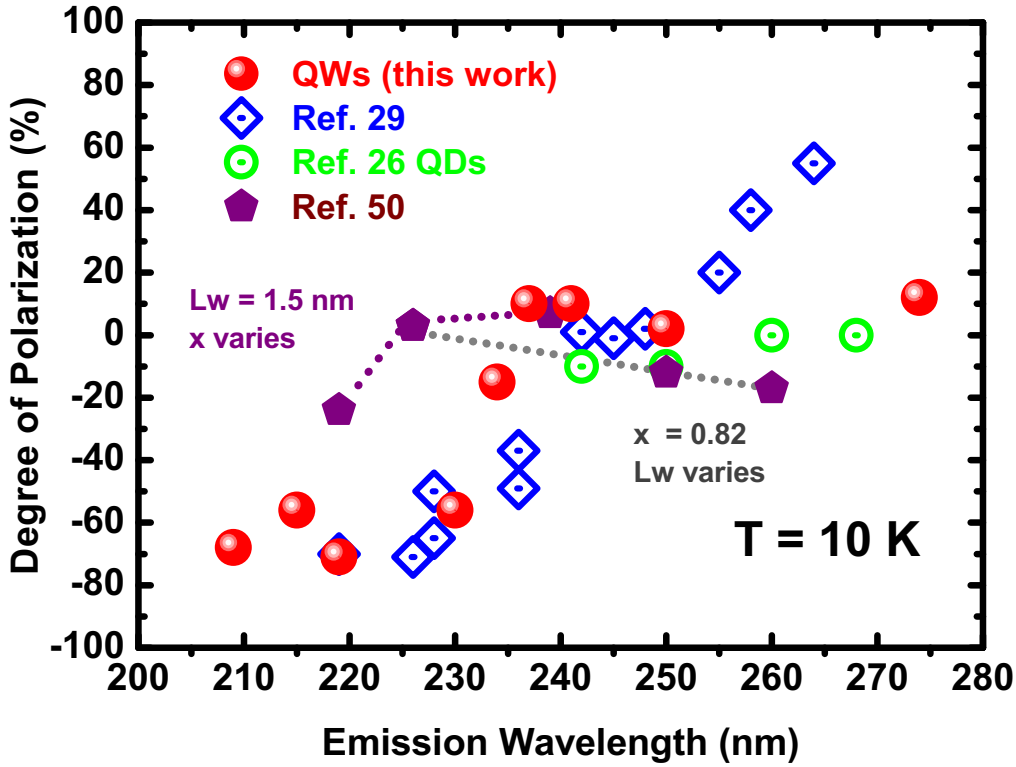

Figure 6: Degree of polarization measured in our $Al_xGa_{1-x}N$ QD and QW samples [body-centered spotted open circles for QDs , reference **26**, red ones for QWs, this work]. Experimental results recorded on samples grown by MOCVD (blue body-centered spotted open diamonds) taken from reference **29**. Data reported in the pioneering work of reference 50 are represented using purple pentagons. The pentagons are bound by a grey (respectively purple) dotted line for (Al,Ga)N QWs grown with similar aluminum composition (respectively well width) and varying well width (respectively aluminum composition).

We then plot in figure 7 the cumulative series of PL energies measured on our series of (Al,Ga)N QWs (purple spheres) and the fluorescence energies reported in ref. 50 (red spheres) versus the nominal aluminum composition of the (Al,Ga)N active regions that are investigated in both works. For comparison, the evolution of the bandgap of the $Al_xGa_{1-x}N$ alloy lattice-matched to AlN is plotted in violet. For the thin confinement layers, i.e. for thicknesses between 1.3 nm and 2 nm, all experimental energies grossly follow the evolution of the bandgap within the possible deviation between the value of the alloy composition where the photons are detected and the nominal value targeted when starting the growth protocols.

This indicates that the contributions of direct and exchange Coulomb effects compensate the confinements or slightly compensate them through this whole series of sample. In the case of reference 50, the observation of QCSE using wider wells and x = 0.82 allows to demonstrate QCSE in agreement with an average experimental value of the energy gradient with the well width of about 720 $keV.cm^{-1}$ through these three samples. For the samples with aluminum compositions greater than 0.6, the optical properties differ only in the broadening of the PL lines, the possibility of observing or not phonon overtones, and the degree of polarization of the edge emissions. Careful examination of the PL spectra in figures 1 and 2 of reference 50 does not reveal any phonon-assisted features at energies lower than the main PL emission, although the aluminum composition of the (Al,Ga)N QWs reaches high enough values to expect them to be observable in accordance with the alloy-induced broadening effects, as we have demonstrated above. Therefore we conclude that alloy broadening effects, which were ignored in the pioneering work of reference 50, may alter its conclusions. Clearly, the complementary mixing of valence band states by local fluctuations of the alloy potential affects the expansion of the excitonic wave functions along the crystalline states to an extent that is different in the two works. Such localized fluctuations of the potential can be correlated either to random distributions of metallic atoms in their sublattice or alternatively to topological defects and nucleation centers (such as threading screw, mixed, edge dislocations, …), or both. In particular, gallium-enriched regions in spirally grown regions of Al-rich (Al,Ga)N alloys have been found to act as carrier localization centers efficiency enhancing the radiative recombination rate **[75]**.

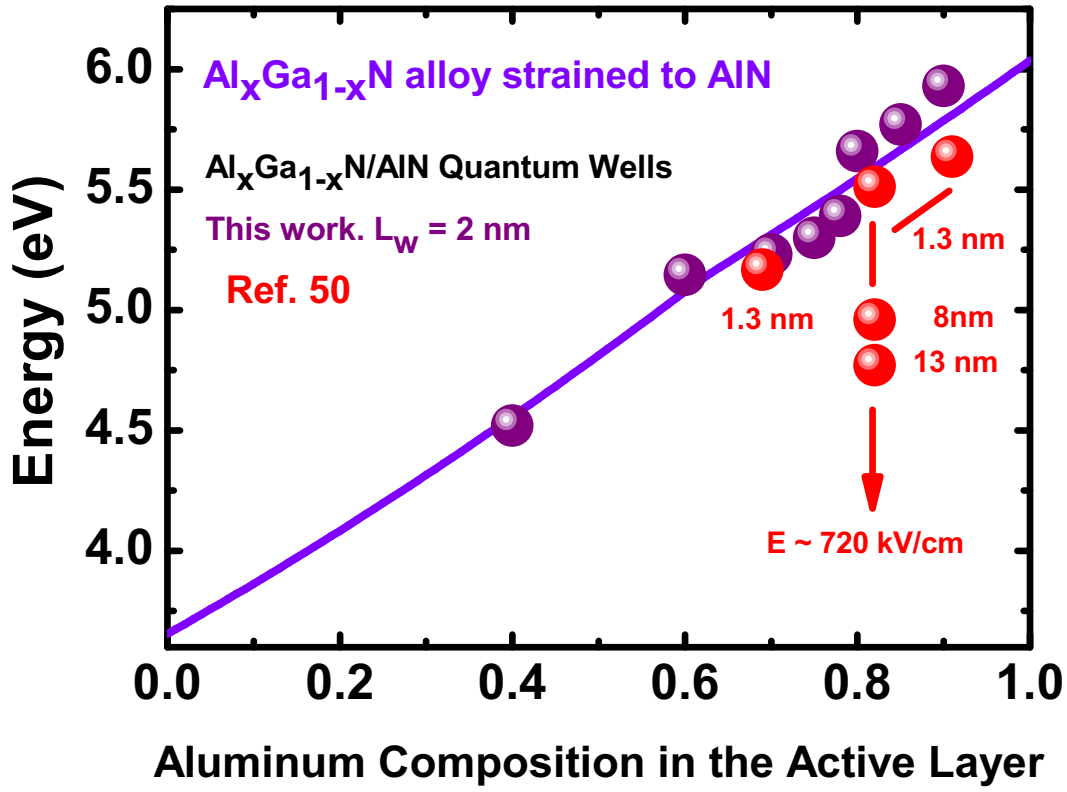

Figure 7: Plot of the PL energies measured on our series of QWs (purple spheres) and the fluorescence energies reported in ref. 50 (red spheres) versus the nominal aluminum composition of the (Al,Ga)N QWs heterostructures that are investigated in both works. The evolution of the bandgap of the $Al_xGa_{1-x}N$ alloy lattice-matched to AlN is plotted in violet. For confining layers with thicknesses ranging between 1.3 nm and 2 nm, the experimental energies grossly follow the evolution of the bandgap. QCSE has been reported for an (Al,Ga)N QWs composition of 0.82 that permits us to estimate an average value of the energy gradient of about 720 keV.cm^{-1} with the well width through these three samples.

Since the early days of quantum mechanics, variational approaches have been used for framing eigen values of complex problems using trial functions, with the following teaching relevant for us here: eigen energies can be obtained with rather close values -although trial functions are dramatically (but reasonably) different. In figure 8 have been reported the relative intensities of the edge emitted PL-emission (a signature of the excitonic wave functions), recorded under the y and z polarization conditions. Once again, the distribution of data through the different series of samples, obtained using different growth protocols, indicates the untrivial interplay between quantum confined stark effects, well-width, direct and exchange coulombic effects and mixings of the traditional Bloch states by the localized fluctuations of the confining potential produced by the (Al,Ga)N alloy disorder. The experimental results dramatically depart from the result of a band-to-band **k.p** calculation of the relative PL intensities in terms of y polarization

(green) and z-polarization (red line) of the emitted photon and cross-over of their contributions for x=0.6. Details in the values of the input parameters (effective masses, bowing parameters, …) cannot be invoked to explain this discrepancy. Experimental results measured on our series of quantum wells (green and red spheres) give a crossover of the intensities for an aluminum composition of (Al,Ga)N of about 0.72% for QW-widths of 2nm in agreement with ref. **50** and compatible with the heuristic theoretical calculation of ref.**24**. The experimental data of reference 50 (full circles for y-polarization and open ones for z-polarization) evidences a contribution of the well-width (series of (Al,Ga)N QWs grown with an Al composition x = 0.82), and a valence band ordering in the alloy (compare data at x=0.69 and x = 0.91). The puzzling lack of global coherence between the different experiments (our work and the pioneering investigation of ref. **50**) is from bona fide attributed to different morphologies of the interfaces, alloy textures and alloy broadening effects. In the perspective of a future unambiguous theoretical disentanglement of the internal quantum efficiency of (Al,Ga)N- based DUV emitting LEDs, this loudly pleads for the need of an accurate, sophisticated calculation of the confined excitonic states through the whole aluminum composition range. The result of such a calculation should be combined with structural investigations of the distributions of the fluctuations of alloy compositions substantially beyond the scope of what has been done hitherto.

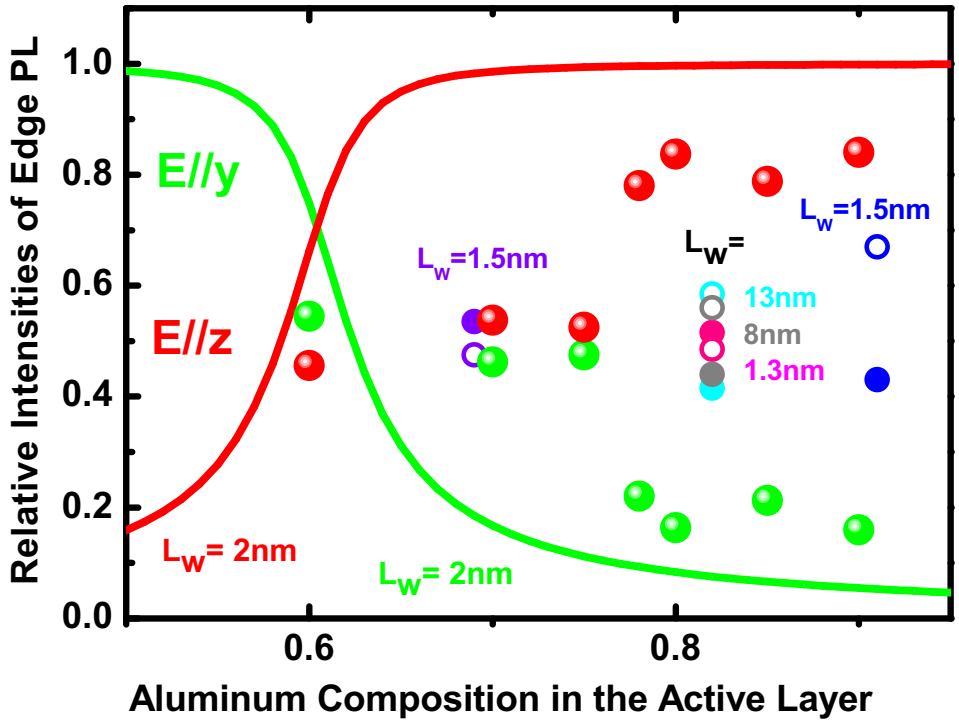

Figure 8: The result of the band-to-band **k.p** calculation of the relative PL intensities in terms of y polarization (green) and z-polarization (red line) of the emitted photon and cross-over of their contributions for x=0.6. Experimental results measured on our series of QWs (green and red spheres) giving a crossover at an aluminum composition of about 0.72% for quantum wells of withs 2nm. The experimental data of reference 50 (full circles for y-polarization and open ones for z-polarization) indicates a contribution of the well width (series of QWs grown with an Al composition of 0.82), and valence band ordering in the alloy (compare data at x=0.69 and x = 0.91).

5. Conclusion and Perspectives.

In conclusion, we have reported the experimental evidence of a substantial loss of TE polarized light emission in the growth plane of UVC emitting LEDs for which the active part of the device is an aluminum-rich (Al,Ga)N-based QW. The evolution of the degree of polarization (here the anisotropy of the amount of light emitted on the edge of the samples) with the shortening of the emission wavelength is similar for these samples grown by MBE to what has been reported for equivalent samples grown by MOCVD, which indicates a maturity of the interface qualities of QWs emitting light in the UVC region. What remains to be done is a comparative measurement of the internal quantum efficiencies in samples grown by both methods. This is tricky, but the recent method proposed by T. Nakano, K. Kawakami, A. A. Yamaguchi **[76]** offers some interesting perspectives. Although the interpretation of the

emission wavelength varies according to the theoretical predictions of a **k.p** calculation, neither the experimental FWHM nor the shapes of the emission diagrams cannot be described. The interpretation of the experimental observations can be explained by taking into account the alloy disorder in (Al,Ga)N and the scattering of carrier through the confined levels of the complex valence sub-band structure of the QWs. A substantial amount of light is emitted in-plane polarized in the on-side growth plane, orthogonally to the growth direction even when forbidden by the **k.p** calculation, for high aluminum compositions of (Al,Ga)N. Based on a phenomenological modelling of the multi-band dispersion relations at the center of the first Brillouin zone, the **k.p** description which follows the predictions of the theory of invariants for wave functions of p and s types (including spin) in case of anions and cations coherently arranged to form a crystal invariant under the full set of the C_{6v}^4 is no longer appropriate for describing the eigenstates and eigenvalues of a disordered system when the disorder cannot be treated as a perturbation of the host Hamiltonian, which is the case here for (Al,Ga)N-AlN QWs. Thanks to the very modest performance of QW LEDs emitting at these very short wavelengths, as the interface morphology is very well-controlled, as indicated by the observation of phonon replica overtones, fully numerical solutions of the kind of those recently proposed for interpreting the performances of (In,Ga)N-based devices **[59,60,77]** are very likely to be explored for improving the light-extraction in UVC light emitting optoelectronic devices. However it is mandatory to develop a holistic many band-approach beyond the scope of the one-band method of reference **[78],** which probably demands some tedious and cumbersome mathematical efforts.

Acknowledgements

Alexandra Ibanez acknowledges the support of the French National Research Agency through the ANR Project ANR-22-CE51-0035 “DOPALGAN” for the funding of her PhD grant. We acknowledge the support by the French National Research Agency through ANR Project GANEX (ANR-11-LABX-0014). GANEX belongs to the publicly funded “Investissements d’Avenir” program managed by the French ANR agency. The authors would like to thank A. Courville, D. Lefebvre, M. Portail B. Poulet, A. Rousseau and S. Vézian, for their invaluable technical and scientific assistance.

References

1-M. Kneissl, T. Y. Seong, J. Han and H. Amano, Nature Photonics, 13, 233 (2019).

2-Christian J Zollner, S P DenBaars, J S Speck and S Nakamura, Semicond. Sci. Technol. 36, 123001 (2021).

3-Walter Harm, Biological Effects of Ultraviolet Radiation , Cambridge University Press, Cambridge, (1980)

4-Manuela Buonanno , Brian Ponnaiya , David Welch , Milda Stanislauskas , Gerhard Randers-Pehrson , Lubomir Smilenov , Franklin D. Lowy , David M. Owens , David J. Brenner, Radiation Research **187**, 493 (2017).

5-Nozomi Yamano, Makoto Kunisada, Sachiko Kaidzu, Kazunobu Sugihara, Aiko Nishiaki-Sawada, Hiroyuki Ohashi, Ai Yoshioka, Tatsushi Igarashi, Akihiro Ohira, Masaki Tanito, Chikako Nishigori **96**, Photochem. Photobiol., 853 (2020).

6-Tomoaki Fukui, Takahiro Niikura, Takahiro Oda, Yohei Kumabe, Hiroyuki Ohashi, Masahiro Sasaki, Tatsushi Igarashi, Makoto Kunisada, Nozomi Yamano, Keisuke Oe, Tomoyuki Matsumoto, Takehiko Matsushita, Shinya Hayashi, Chikako Nishigori, Ryosuke Kuroda, PLoS One **15**, e0235948 (2020).

6-Yoshihiko Muramoto, Masahiro Kimura and Suguru Nouda, Semicond. Sci. Technol. **29**, 084004 (2014).

7-Aurélien David, Nathan G. Young, Cory Lund and Michael D. Craven, ECS Journal of Solid State Science and Technology, **9**, 016021, (2019).

8-Douglas N. Arnold, Guy David, David Jerison, Svitlana Mayboroda, and Marcel Filoche Phys. Rev. Lett. **116**, 056602 (2016).

9-Marcel Filoche, Marco Piccardo, Yuh-Renn Wu, Chi-Kang Li, Claude Weisbuch, and Svitlana Mayboroda Phys. Rev. B **95**, 144204 (2017).

10-Chi-Kang Li, Marco Piccardo, Li-Shuo Lu, Svitlana Mayboroda, Lucio Martinelli, Jacques Peretti, James S. Speck, Claude Weisbuch, Marcel Filoche, and Yuh-Renn Wu Phys. Rev. B **95**, 144206 (2017).

11-W. Hahn, J.-M. Lentali, P. Polovodov, N. Young, S. Nakamura, J. S. Speck, C. Weisbuch, M. Filoche, Y. R. Wu, M. Piccardo, F. Maroun, L. Martinelli, Y. Lassailly, and J. Peretti Phys. Rev. B **98** (2018).

12-Optical Processes in Semiconductors, Jacques I. Jacques Pankove, dover publications inc. New York (1971).

13-M. L. Nakarmi, K. H. Kim, J. Li, J. Y. Lin, and H. X. Jiang, Applied Physics Letters **82**, 3041 (2003).

14-John L. Lyons, Anderson Janotti, and Chris G. Van de Walle, Phys. Rev. Lett. **108**, 156403 (2012).

15-Pegah Bagheri, Andrew Klump, Shun Washiyama, M. Hayden Breckenridge, Ji Hyun Kim, Yan Guan,Dolar Khachariya, Cristyan Quiñones-García, Biplab Sarkar, Shashwat Rathkanthiwar, Pramod Reddy, Seiji Mita, Ronny Kirste, Ramón Collazo, Zlatko Sitar, Appl. Phys. Lett. **120**, 082102 (2022).

16-F. Piva, M. Grigoletto, D. Hauer Vidal, M. Guttmann, G. Meneghesso, E. Zanoni, R. Brescancin, C. De Santi, J. Rass, S. Einfeldt, M. Meneghini, M. Buffolo, J. Ruschel, J. Glaab, M. Kneissl, Appl. Phys. Lett. **122**, 151108 (2023).

18-Yuxuan Chen, Jianwei Ben, Fujun Xu, Jinchai Li, Yang Chen, Xiaojuan Sun, Dabing Li, Fundamental Research **1**, 717 (2021).

19- H. Hirayama, N. Noguchi, T. Yatabe, and N. Kamata, Appl. Phys. Express **1**, 051101 (2008).

20-M. Leroux, S. Dalmasso, F. Natali, S. Helin, C. Touzi, S. Laügt, M. Passerel, F. Omnes, F. Semond, J. Massies, and P. Gibart, Phys. Stat. Sol. (b) **234**, 887 (2002).

21-K. B. Nam, J. Li, M. L. Nakarmi, J. Y. Lin, and H. X. Jiang, Appl. Phys. Lett. **84**, 5264 (2004).

22-Yoshitaka Taniyasu and Makoto Kasu, Applied Physics Letters **99,** 251112 (2011).

23-Alexandra Ibanez, Nikita Nikitskiy, Aly Zaiter, Pierre Valvin, Wilfried Desrat, Thomas Cohen, M. Ajmal Khan, Guillaume Cassabois, Hideki Hirayama, Patrice Genevet, Julien Brault, and Bernard Gil, Journal of Applied Physics **134**, 193103 (2023) and references therein.

24- A.Yamaguchi, Phys. Status Solidi (c) **5**, 2364 (2008).

25-A. Yamaguchi, Appl. Phys. Lett. **96**, 151911 (2010).

26-Martin Feneberg , Fátima Romero ,Rüdiger Goldhahn ,Tim Wernicke ,Christoph Reich, Joachim Stellmach; Frank Mehnke Appl. Phys. Lett. **118**, 202101 (2021)

27-Tim Kolbe, Arne Knauer, Chris Chua, Zhihong Yang, Sven Einfeldt, Patrick Vogt, Noble M. Johnson, Markus Weyers, Michael Kneissl, Applied Physics Letters **97**, 171105 (2010).

28-J. E. Northrup, C. L. Chua, Z. Yang, T. Wunderer, M. Kneissl, N. M. Johnson, and T. Kolbe Applied Physics Petters **100**, 021101 (2012).

29-Martin Guttmann, Frank Mehnke, Bettina Belde, Fynn Wolf, Christoph Reich, Luca Sulmoni, Tim Wernicke, and Michael Kneissl, Jpn. J. Appl. Phys. **58**, SCCB20 (2019).

30-H. Wang, L. Fu, H. M. Lu, X. N. Kang, J. J. Wu, F. J. Xu, and T. J. Yu, Optics express **27**, A436 (2019) and references therein.

31-B. Neuschl, J. Helbing, M. Knab, H. Lauer, M. Madel, K. Thonke, T. Meisch, K. Forghani, F. Scholz, and M. Feneberg, Journal of Applied Physics **116**, 113506 (2014).

32-Christoph Reich, Martin Guttmann, Martin Feneberg, Tim Wernicke, Frank Mehnke, Christian Kuhn, Jens Rass, Mickael Lapeyrade, Sven Einfeldt, Arne Knauer, Viola Kueller, Markus Weyers, Rüdiger Goldhahn, and Michael Kneissl, Appl. Phys. Lett. **107**, 142101 (2015).

33-Hirotsugu Kobayashi, Shuhei Ichikawa, Mitsuru Funato, Yoichi Kawakami, Advanced Optical Materials **7**, 1900860 (2019).

34-P.A. Shields, R.J. Nicholas, N. Grandjean, and J .Massies, Phys.Rev. B **63**, 245319, (2001).

35-S. Chichibu, A. Shikanai, T. Azuhata, and T. Sota, A. Kuramata and K. Horin, S. Nakamura, Appl. Phys. Lett. **68** 3766,(1996).

3§-K. Kornitzer, T. Ebner, K. Thonke, and R. Sauer, C. Kirchner, V. Schwegler, and M. Kamp, M. Leszczynski, I. Grzegory, and S. Porowski, Phys. Rev. B **60**, 1471, (1999).

37-K. Torii, T. Deguchi, T. Sota, K. Suzuki, S. Chichibu, and S. Nakamura, Phys. Rev. B **60**, 4723 (1999) .

38-E. Silveira, J. A. Freitas, Jr., O. J. Glembocki, G. A. Slack, and L. J. Schowalter Phys. Rev. B **71**, 041201,(2005).

39-G.Rossbach, M. Feneberg, M.Roppischer, C. Werner, N. Esser, C. Cobet, T. Meisch, K. Thonke, A. Dadgar, J. Blasing, A. Krost, and R. Goldhahn Phys. Rev. B **83**, 195202 (2011).

40-H.Lahreche, M. Leroux, M. Laugt, M. Vaille, B. Beaumont, P. Gibart, Journal of Applied Physics **87**, 577, (2000).

41-Symmetry and Strain-induced effects in semiconductors, by G (John Wiley and Sons, Gennadiĭ Levikovich Bir and Gregory Ezekielevich Pikus, (1974). ISBN 0470073217.

42-K. Cho, Phys. Rev. B **14**, 4463, (1976).

43-Kobayashi, O. F. Sankey, S. M. Volz, and J. D. Dow. Phys. Rev. B **28**, 935 (1983).

44-Masakatsu Suzuki, Takeshi Uenoyama, and Akira Yanase Phys. Rev. B **52**, 8132 (1995).

45-S.L.Chuang and C.S.Chang, Phys.Rev. B **54**, 2491 (1996).

46-K. Kim, W. R. L. Lambrecht, and B. Segall, Phys. Rev. B **53**, 16310, (1996), Erratum: Phys. Rev. B **56**, 7018 (1997).

47-K.Kim, W.R.L.Lambrecht, B. Segall, and M. van Schilfgaarde. Phys. Rev. B **56**, 7363 (1997).

48-M. Kumagai, S. L. Chuang, and H. Ando, Phys. Rev. B **57**, 15303 (1998).

49-P. Rinke, M. Winkelnkemper, A. Qteish, D. Bimberg, J. Neugebauer, and M. D.

Scheffler. Phys. Rev. B **77**, 075202 (2008).
50-R. Banal, M.Funato and Y Kawakami, Physical Review B **79**, R121308(R) (2009).
51-T. Kolbe, A. Knauer, C.L.Chua, Zhihong Yang, S. Einfeldt, P. Vogt, N.M.Johnson, M. Weyers and M. Kneissl, Applied Physics Letters **97**, 171105 (2010).
52-J.E. Northrup, C.L. Chua, Zhihong Yang, T. Wunderer, M. Kneissl, N.E. Johnson and T. Kolbe, Applied Physics Letters **100**, 021101 (2010).
53-M.Feneberg, M. Winkler, J.Klamser, J.Stellmach, M. Frentrup, S. Ploch, F. Mehnke, T.Wernicke, M. Kneissl and R. Goldhahn, Applied Physics Letters **106**, 182102 (2015).
54-H. Wang, L. Fu, H. M. Lu, X. N. Kang, J. J. Wu, F. J. Xu, and T. J. Yu, Optics express **27**, A436 (2019) and references therein.
55-Seoung-Hwan Park, Jongmyeong Kim, Doyeol Ahn and Euijoon Yoon, Physica E **120**, 114112 (2020).
56-Yuxuan Chen, Jianwei Ben, Fujun Xu, Jinchai Li, Yang Chen, Xiaojuan Sun, Dabing Li, Fundamental Research **1**, 717 (2021).
57-R. Ishii, A. Kaneta, M. Funato, and Y. Kawakami, Phys. Rev. B **81**, 155202, (2010).
58-R. Ishii, A. Kaneta, M. Funato, and Y. Kawakami, Phys. Rev. B **87**, 235201, (2013).
59-Aurélien David, Phys. Rev. Applied **15**, 054015 (2021).
60-Aurélien David and Claude Weisbuch, Phys. Rev. Research **4**, 043004 (2022).
61-E. P. Pokatilov, D. L. Nika, V. M. Fomin, and J. T. Devreese, Phys. Rev. B **77**, 125328 (2008).
62-Properties of the Thirty-Two Point Groups," G. F. Koster, J. O. Dimmock, R. G. Wheeler and H. Statz, MIT Press, Cambridge, (1964)**.**
63-Hideki Hirayama, Sachie Fujikawa, Norimichi Noguchi1, Jun Norimatsu,Takayoshi Takano, Kenji Tsubaki, and Norihiko Kamata, Phys. Status Solidi (A) **206**, 1176 (2009).
64-M.A. Khan, N. Maeda, J. Yun, M. Jo, Y.Yamada and H. Hirayama Sci Rep **12**, 2591 (2022).
65-T. Q. P. Vuong, G. Cassabois, P. Valvin, V. Jacques, A. Van Der Lee, A. Zobelli, K. Watanabe, T. Taniguchi and B. Gil, 2D Mater. **4** (2017) 011004.
66-G.Rossbach, M. Feneberg, M.Roppischer, C. Werner, N. Esser, C. Cobet, T. Meisch, K. Thonke, A. Dadgar, J. Blasing, A. Krost, and R. Goldhahn Phys. Rev. B **83**, 195202 (2011).
67-B.Halperin and M Lax, Phys. Rev. **148,** 722 (1966).
68-S.D. Baranowski, A.L. Efros, Sov. Phys. Semicond. **12** 1328 (1978)
69-Sergei D. Baranovskii, Alexey V. Nenashev, Dirk Hertel, Florian Gebhard, and Klaus Meerholz, ACS Omega **7**, 45741 (2022).

70-S. Kalliakos, T. Bretagnon, P. Lefebvre, T. Taliercio, B. Gil, N. Grandjean,B. Damilano, A. Dussaigne and J. Massies, J. Appl. Phys. **96**, 180 (2004)

71-T. Bretagnon, P. Lefebvre, P. Valvin, R. Bardoux, T. Guillet, T. Taliercio, B. Gil, N. Grandjean, F. Semond, B. Damilano, A. Dussaigne, and J. Massies, Phys. Rev. B **73**, 113304 (2006)

72-Mathieu Leroux, unpublished

73-Bernard Gil, in Physics of Wurtzite Nitrides and Oxides: Passport to Devices, ISSN 0933-033X, ISBN 978-3-319-06804-6, DOI 10.1007/978-3-319-06805-3, springer Heidelberg New York Dordrecht London, ISSN 2196-2812 (electronic) ISBN 978-3319-06805-3 (eBook), Springer International Publishing Switzerland (2014).

74-M. Moret, B. Gil, S. Ruffenach, O. Briot, Ch. Giesen, M. Heuken, S. Rushworth, T. Leese, M. Succi, Journal of Crystal Growth **311**, 2795 (2009)**.**

75- M.Funato, R.G.Banal and Y.Kawakami, AIP Advances 5, 117115 (2015).

76- T. Nakano, K. Kawakami, A. A. Yamaguchi Proceedings Volume **9748**, Gallium Nitride Materials and Devices XI; 97481W (2016).

77-Yoshitaka Taniyasu and Makoto Kasu, NTT technical review, Special Feature: Frontline Materials Research **8**,1 (2010).

78- Tsung-Yin Tsai, Kai Shek Qwah, Jean-Philippe Banon, Marcel Filoche, Claude Weisbuch, Yuh-Renn Wu, and James S. Speck, Physical Review Applied **20**, 044069 (2023).

FIGURE CAPTIONS

Figure 1: (a) and (b) : AFM images of the surface morphology of AlN template on c-plane sapphire substrate with (a) 5 µm×5 µm and (b) 1 µm×1 µm scan areas. (c) AFM image of the surface after the growth of an (Al,Ga)N QW with an aluminum composition of 70%. The scale of the insert of figure 1-(c) is 1 µm×1 µm. The value of the root mean square (RMS) roughness is 0.2 nm with an average terrace width of 70±20 nm.The step height is 1 monolayer.

Figure 2: Normalized PL spectra of six QWs for aluminum nominal compositions of the (Al,Ga)N confining alloys of 40% (blue) , 60% (orange), 70% (green) ,75%, (magenta), 78% (dark grey) , 80% (violet), 85% (green) and 90% (silver). Note the AlN emission at 205 nm. PL spectra were recorded either in conditions of below barrier energy photo-excitation at 213 nm, and above barrier photo-excitation at 196 nm, as indicated in the figure.

Figure 3: (a) PL spectrum (violet) of the 80% QW and its line-shape fitting (green) using a gaussian function with a value of the σ parameter of 29 meV and Huang-Rhys factor S = 0.4. (b) PL spectrum (silver) of the 90% QW with zero-phonon emission at 209 nm and its line-shape fitting (red) using gaussian function with a value of the σ parameter of 20 meV and Huang-Rhys factor S = 0.16. Please note the narrower AlN emission at 205 nm.

Figure 4: (a) Evolution of the quantity E_0 (x), which characterizes the strength of the alloy-induced broadening obtained using equation 1 (blue). The numerical calculation in blue was done with the following parameters: $E_g(Al_xGa_{1-x}N) = 6.2x+3.4(1-x) – bx(1-x)$ with b = 0.8±0.2 eV , which gives $\alpha = 2(1+ 0.8x)$; $N = 4.38\ 10^{28}\ m^{-3}$ and the value of M was averaged to M = 1.5 in units of the electron mass at rest through the whole composition range. Calculation in magenta corresponds to a value of b = 0.9 eV. The red spheres represent the evolution of the FWHM of the high energy part of the PL features of the different (Al,Ga)N QWs. The green spheres correspond to PL emissions recorded on thick non-intentionaly doped AlGaN layers grown by MOVPE on sapphire substrates **[72]**. **(b)** Evolution of the valence band energies versus the aluminum composition in case of (Al,Ga)N lattice-matched to AlN (black, red and blue) together with a representation of the alloy broadening effect (values of E_0) in dark green.

FIGURE 5: (a) Emission diagrams of the QWs with different Al compositions. A similar color code is associated to the different samples in figure 2 and figure 5(a).The directions of the y and z axis are indicated in the left-hand bottom corner. **(b)** Plot of the PL spectra recorded for the 80% Al composition (Al,Ga)N QW sample for the y (green plot) and z (red plot) polarizations of the on-side emission. **(c)** PL emitted under z (red plot) polarization and under y (black plot) polarization conditions. The black feature is magnified by a factor 5.2 which corresponds to a DOP of -68 percent.

Figure 6: Degree of polarization measured in our $Al_xGa_{1-x}N$ QD and QW samples [body-centered spotted open circles for QDs , reference **26**, red ones for QWs, this work]. Experimental results recorded on samples grown by MOCVD (blue body-centered spotted open diamonds) taken from reference **29**. Data reported in the pioneering work of reference 50 are represented using purple pentagons. The pentagons are bound by a grey (respectively purple) dotted line for (Al,Ga)N QWs grown with similar aluminum composition (respectively well width) and varying well width (respectively aluminum composition).

Figure 7: Plot of the PL energies measured on our series of QWs (purple spheres) and the fluorescence energies reported in ref. 50 (red spheres) versus the nominal aluminum composition of the (Al,Ga)N QWs heterostructures that are investigated in both works. The evolution of the bandgap of the $Al_xGa_{1-x}N$ alloy lattice-matched to AlN is plotted in violet. For confining layers with thicknesses ranging between 1.3 nm and 2 nm, the experimental energies grossly follow the evolution of the bandgap. QCSE has been reported for an (Al,Ga)N QWs composition of 0.82 that permits us to estimate an average value of the energy gradient of about 720 $keV.cm^{-1}$ with the well width through these three samples.

Figure 8: The result of the band-to-band **k.p** calculation of the relative PL intensities in terms of y polarization (green) and z-polarization (red line) of the emitted photon and cross-over of their contributions for x=0.6. Experimental results measured on our series of QWs (green and red spheres) giving a crossover at an aluminum composition of about 0.72% for quantum wells of withs 2nm. The experimental data of reference 50 (full circles for y-polarization and open ones for z-polarization) indicates a contribution of the well width (series of QWs grown with an Al composition of 0.82), and valence band ordering in the alloy (compare data at x=0.69 and x = 0.91).